Chapter 1 Introduction

1.1 Photonic Crystal Microcavity Laser

The concept of photonic crystal was first proposal by E. Yablonovitch in 1987 [1], which means the material with periodic refractive index arrangement. By using various fabrication processes, one can obtain and design various photonic crystal. The most important and famous feature of photonic crystal is its photonic band-gap (PBG). In PBG region, light with specific frequency range will be reflected and scattered. In the other words, the light propagation will be forbidden. This feature also opens the possibility for human beings to control the photon flow by inducing some defects, for example, microcavities and waveguides. Generally, the typical photonic crystal can be classified into one dimensional (1D), two dimensional (2D), and three dimensional (3D) according to their dimensions of periodic arrangement, as shown in Fig. 1. 1. Actually, over 100 years ago, the first 1D photonic crystal has been proposed by William H. Bragg, which is known as the distribution Bragg reflection (DBR) and still widely used in semiconductor lasers, for example, vertical-cavity surface-emission lasers (VCSELs). Recently, 2D and 3D photonic crystal have attracted lots of attentions and been widely investigated.

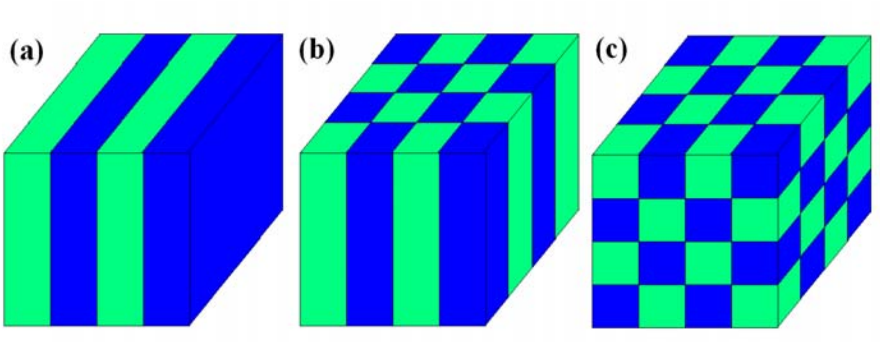

Fig. 1. 1: The scheme of (a) 1D, (b) 2D, and (c) 3D photonic crystal.

Comparing 2D with 3D photonic crystal, it is much easier to fabricate for the former one. Thus, 2D photonic crystal has been widely employed in various applications in recent years, including fiber [2], semiconductor lasers [3], waveguide devices, light emitting diode (LED) [4], photonic integrated circuits (PICs) [5], and so on. Generally, in most cases in semiconductor materials, the photonic crystal pattern is usually defined on photo resist by electron-beam lithography, photo lithography, or nanoimprint. And then, the photonic crystal pattern will be further transferred to the silicon or III-V compound material by various dry-etching processes, for example, reactive ion-etching (RIE), ion-couple plasma (ICP) dry-etching, and chemically assisted ion beam etching (CAIBE). The related fabrication processes also become mutual in recent years.

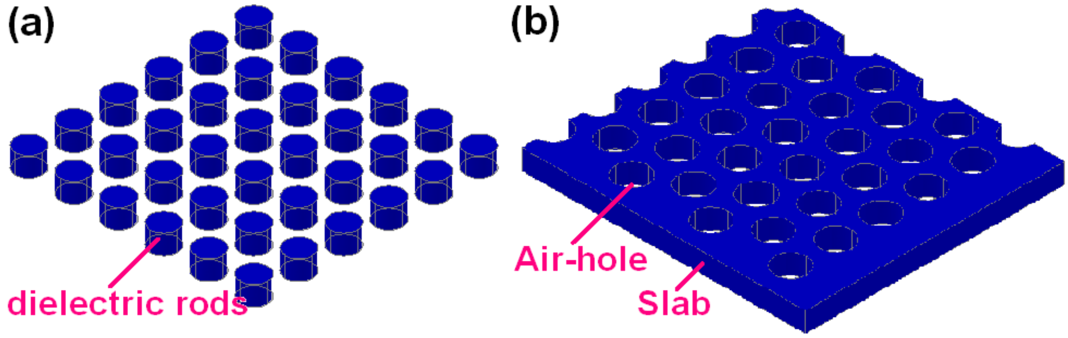

Fig. 1. 2: The scheme of photonic crystal composed by (a) dielectric rods and (b) air-holes on slab structure.

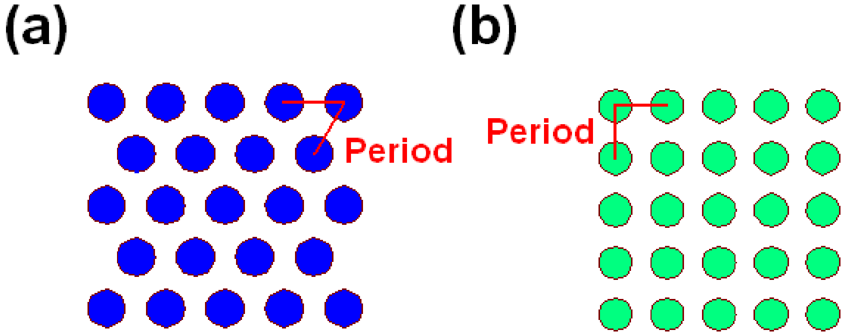

Fig. 1. 3: The scheme of photonic crystal with (a) triangular and (b) square lattice structure.

Generally, 2D photonic crystals can be divided into air-holes on dielectric slab and dielectric-rods structures as shown in Fig. 1. 2, which usually show transverse electric (TE) and transverse magnetic (TM) PBG, respectively. The square and triangular lattice photonic crystals with low symmetry shown in Fig. 1. 3 [6] [7] have been widely used in various applications. For certain lattice parameter design, PBG with large frequency range can be easily obtained from triangular and square lattice photonic crystals in TE- and TM-like mode as shown in Fig. 1. 4 (a) and (b). Besides, very recently, there also some special photonic crystal lattice structures with higher symmetry, which are come from the concept of quasi-crystal lattice, for example, octagonal, dodecagonal and circular photonic crystals. Large PBG can also be found

As we mention before, photonic crystal can be served as perfect mirror for the light with frequency in PBG region. Hence, the property can be employed in many applications such as microcavities and waveguides. Take microcavity for example, as shown in Fig. 1. 5, the photonic crystal is formed by air holes on dielectric slab and the cavity region is formed by removing several air holes. Due to the mirror effect provided in in-plane direction by photonic crystal and the total-internal reflection (TIR) in vertical direction, the photons will be confined and many localized modes will resonate in the cavity region.

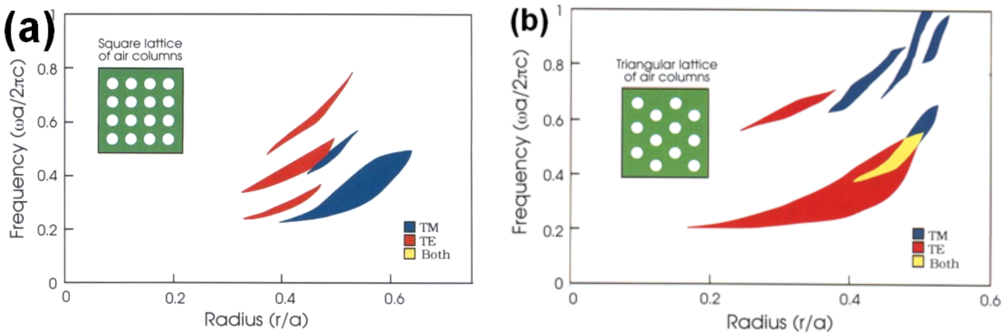

Fig. 1. 4: The PBG gap map of (a) square and (b) triangular lattice photonic crystal compose by air holes on dielectric medium with dielectric constant of 11.4.[8]

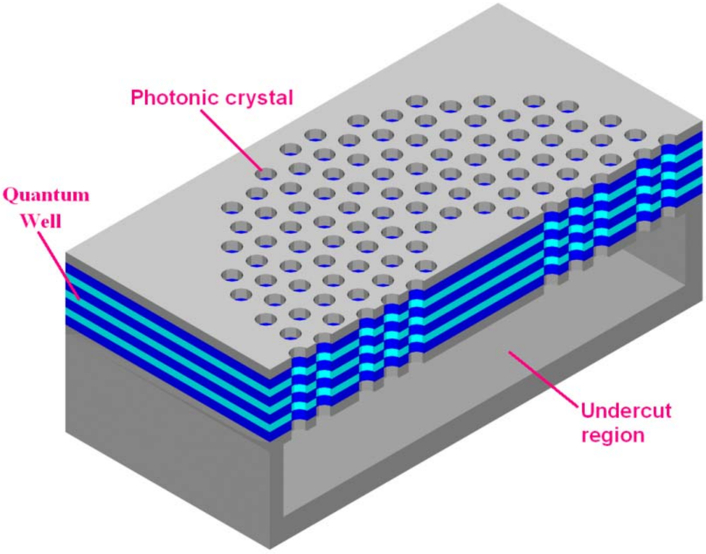

Fig. 1. 5: The scheme of photonic crystal microcavity formed on membrane structure.

Comparing with general semiconductor lasers, photonic crystal microcavity laser shows lots excellent properties, including ultra high quality (Q) factor, ultra low threshold, extreme small mode volume, and high spontaneous emission (β) factor. Lots of amazing achievement has been reported in recent years. Up to date, for example, the smallest mode volume of 2.1 $(\lambda/n)^3$ from photonic crystal point-shift microcavity is achieved and reported by K. Nozaki *et al.* [9], as shown in Fig. 1. 6 (a). Besides, the highest measured Q factor of 900,000 from point-shifted photonic crystal waveguide double heterostructure microcavity is also reported by M. Notomi *et al.* [10], as shown in Fig. 1. 6 (b). Besides, either modify the lattice constant (a) or air-hole radius (r) versus lattice constant (r/a) ratio can change the wavelength of the localize modes and PBG region. Besides, one can tune the air-holes size or position near the cavity to control the modal properties and symmetric of localized modes easily. Although lots properties have been clearly investigated, there still some bottlenecks and issues should be

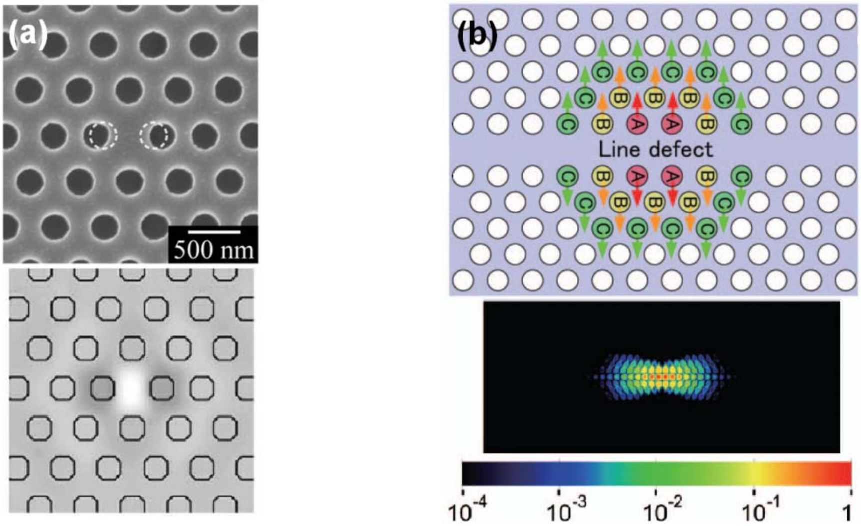

Fig. 1. 6: (a) The point-shifted photonic crystal cavity with ultra-small mode volume by K. Nozaki *et al* [9]. (b) The photonic crystal waveguide point-shifted microcavity with ultra-high measured *Q* factor by M. Notomi *et al* [10].

broken through and addressed in membrane structure photonic crystal microcavity lasers.

1. **It is difficult to achieve electrically driven photonic crystal microcavity laser. Most photonic crystal microcavity lasers in present researches are excited by optical pumping.**
2. **Besides, due to the poor heat sink of air-cladding in membrane structure, it is still difficult to achieve continuous wave (CW) lasing. Although there have been several reports of CW lasing actions from photonic crystal microcavities (microcavity size < 3 μm), there is still leaking of proper electrically driven structure in these reports.**

In my thesis, I will focus on solving these two issues at the same structure.

1.2 Motivation: Achieve Electrically Driven and Improve Heat Sinking

From past related researches, the concept of inserting a central post under the microcavity [11] originated from micro-disks [12] has been regarded as a promising solution to solve above problem. For resonance modes with central zero field distributions, for example, whispering-gallery (WG) mode, the inserted central post can be efficiently served as a current injection pathway with relatively slight influences on the lasing performance. Furthermore, the post also plays the roles of heat sinker. The first demonstration of electrically-driven photonic crystal microcavity laser with monopole mode using the central post structure is achieved by H. G. Park *et al*. [12], as shown in Fig. 1.7. Very recently, the electrically-driven lasing actions of WG (hexapole) mode using the same structure are also achieved and reported by the same group [13]. Even so, adding a central post under the microcavity without affecting the lasing mode is still very crucial and can be further improved both in structure design and fabrication tolerances. Besides, the thermal properties when inserting a central post have not been investigated clearly yet. We believe the microcavity with central post structure based on WG mode plays the key role towards electrically-driven CW operated photonic crystal lasers.

In my thesis, we will apply the dodecagonal (12-fold) quasi-photonic crystal (QPC) D_2 microcavity formed by removing seven air holes. There are two main advantages in design

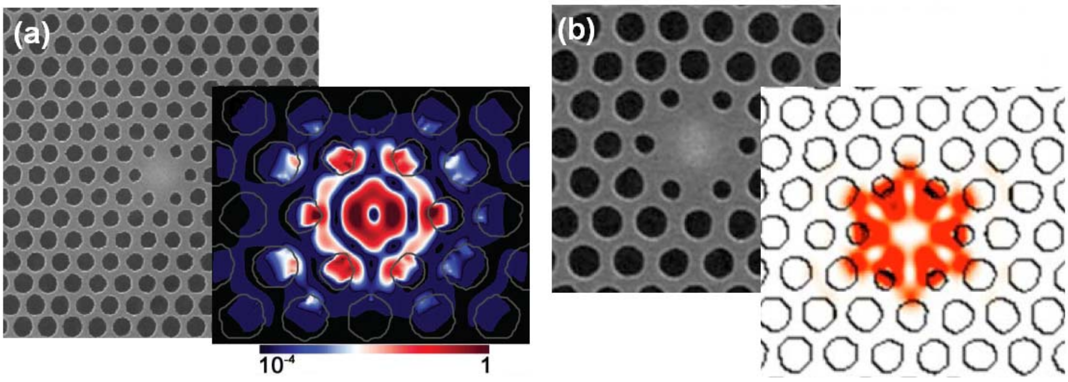

Fig. 1. 7: The electrically-driven photonic crystal microcavity structure based on monopole and hexapole mode by Prof. Y. H. Lee's group in KAIST.

and fabrications to apply 12-fold QPC D_2 microcavity in my researches. First, the WG mode with high quality (*Q*) factor can be easily sustained in this microcavity. We do not choose other photonic crystal microcavity such as L3 cavity with ultra-high *Q* factor or point shifted nanocavity with very small mode volume. Because their mode profile without central field distribution node are not suitable for electrically driven by the central post structure. Second, it is un-necessary to design windows when fabricating the central post in this microcavity design due to its lattice structure, which is a very convenient feature in fabrications. If the window is applied, it will be much difficult to design the electrode.

In addition to current injection issue, the post can also play the role of heat sinker in the microcavity. The thermal conductivity of the InP central post under the microcavity is much larger than that of air. Considering that the central post is not large enough to arise any significant optical losses from WG mode, the most heat flow due to non-radiative carrier recombination in the microcavity region will be transferred into substrate by the central post. And then the temperature in the cavity region will be reduced, which shows the potential of CW lasing operations.

Although our proposed cavity size here is larger than that in ref [14], the heat sink, Q factors, electrical resistances, and fabrication tolerance can all be better.

1.3 Overview

In this thesis, in chapter 2, we will investigate the influences on WG mode in 12-fold microcavity caused by the post by using finite-difference time-domain (FDTD) and finite-element method (FEM). These will include Q factor variation, thermal properties, and their trade-off in design. In chapter 3, the fabrication process of electrically-driven photonic crystal microcavity structure will be illustrated. And the setup of micro-electric-luminescence (micro-EL) measurement system and EL measurement results will also illustrated in chapter 3. Finally, there will be brief conclusion in chapter 4.

Chapter 2 Quality Factor and Heat Sink of 12-Fold QPC D_2 Microcavity with Different Central Post Sizes

2.1. Introduction

In this chapter, we focus our researches on the *Q* factors and heat sink improvement of 12-fold QPC D_2 microcavity formed by removed seven air-holes by inserting central posts with different sizes under the microcavity. At first, I will calculate *Q* factor with different post size by finite-difference time-domain (FDTD) method. And then the heat sink improved by different central posts will be also investigated in simulations. In simulations, I will employ finite element method (FEM) to calculate heat dissipation with different post size in detail. The membrane structure is difficult to achieve CW lasing due to the poor heat dissipation of the air-cladding. When the pumped laser is with large duty circle, the temperature of the membrane microcavity will be increased. Thus, we will also investigate the possibility of achieving CW lasing action by the central post structure microcavity. The simulated results and discussions will be shown in this chapter.

2.2. *Q* Factor Varied by Different Post Sizes

2.2.1. Finite-Difference Time-Domain Method

In the calculation method, we are difficult to divide the domain into infinite area. For example, each area is equal to $\Delta X \cdot \Delta Y$ in 2D transverse magnetic wave (TM). According to

Maxwell's equation (1), (2):

$$\nabla \times \vec{E} = -\frac{\partial \vec{B}}{\partial t} - \sigma_m \vec{H} - \vec{M} \tag{1}$$

$$\nabla \times \vec{H} = \frac{\partial \vec{D}}{\partial t} + \sigma_e \vec{E} + \vec{J}) \tag{2}$$

We divide the simulation domain into Yee's cells. The electric and magnetic field are separated. There is a point in the center of the Yee's cell. Electric field is in the center, and magnetic field is around the electric field. The magnetic field is changed by electric field with time. The electric field in the same position is formed by the electric and magnetic on last time step. We divide the Maxwell's equation into equation (4) and (5) by central difference method.

$$\begin{aligned} E_z(i,j,n+\frac{1}{2}) &= E_z(i,j,n-\frac{1}{2})\left[\frac{2\varepsilon_{(i,j)}-\sigma_{e(i,j)}\Delta t}{2\varepsilon_{(i,j)}+\sigma_{e(i,j)}\Delta t}\right]+\left[\frac{2\Delta t}{2\varepsilon_{(i,j)}+\sigma_{e(i,j)}\Delta t}\right] \\ &\cdot\left\{\frac{1}{\Delta x}[H_y(i+\frac{1}{2},j,n)-H_y(i-\frac{1}{2},j,n)]-\frac{1}{\Delta y}[H_x(i,j+\frac{1}{2},n)-H_x(i,j-\frac{1}{2},n)]-J_Z(i,j,n)\right\} \end{aligned} \tag{3}$$

$$\begin{aligned} H_x(i,j+\frac{1}{2},n+1) &= H_x(i,j+\frac{1}{2},n)\left[\frac{2\mu_{(i,j+\frac{1}{2})}-\sigma_{m(i,j+\frac{1}{2})}\Delta t}{2\mu_{(i,j+\frac{1}{2})}+\sigma_{m(i,j+\frac{1}{2})}\Delta t}\right] \\ &-\frac{2\Delta t}{\Delta y(2\mu_{(i,j+\frac{1}{2})}+\sigma_{m(i,j+\frac{1}{2})}\Delta t)}[E_z(i,j+1,n+\frac{1}{2})-E_z(i,j,n+\frac{1}{2})] \end{aligned} \tag{4}$$

$$\begin{aligned} H_y(i+\frac{1}{2},j,n+1) &= H_y(i+\frac{1}{2},j,n)\left[\frac{2\mu_{(i+\frac{1}{2},j)}-\sigma_{m(i+\frac{1}{2},j)}\Delta t}{2\mu_{(i+\frac{1}{2},j)}+\sigma_{m(i+\frac{1}{2},j)}\Delta t}\right] \\ &+\frac{2\Delta t}{\Delta x(2\mu_{(i+\frac{1}{2},j)}+\sigma_{m(i+\frac{1}{2},j)}\Delta t)}[E_z(i+1,j,n+\frac{1}{2})-E_z(i,j,n+\frac{1}{2})] \end{aligned} \tag{5}$$

The *i* and *j* means the value of the coordinates and n is the time step. The electric and magnetic field is expanded by the Fourier Transform in the above equation. In real simulation, the domain is finite. When the artificial boundary is formed, there will be produced the

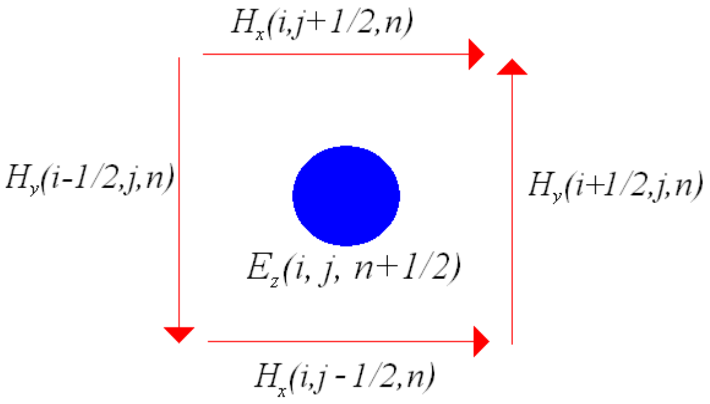

Fig. 2.1: The illustration of FDTD calculation.

reflection of electric and magnetic field on the boundary. Thus, we will add a Perfect matched layer (PML) outside the domain boundary. The PML can regard as good conductivity. It can reduce the amplitude and reflection in the PML. We can reduce the reflection effects of the electric and magnetic field by the PML.

2.2.2. Q Factor with Different Central Post Sizes by 3D FDTD

In order to achieve electrically pumped structure, we will insert a post under the center of microcavity. The most localize modes in 12-fold QPC D_2 microcavity will be affected and destroyed by the large post size. Thus, the $WG_{6,1}$ mode in this microcavity will be the best choice due to its zero-field distribution, where the former and later sub-number denotes the azimuthal number and the order of radiation of WG mode, respectively, as shown in Fig. 2. 2. However, due to the following related researches, it is necessary to know that how large central post size will affect the $WG_{6,1}$ mode. Thus, we will investigate this problem in details, which will be an important design reference when the structure is applied to electrically pumping.

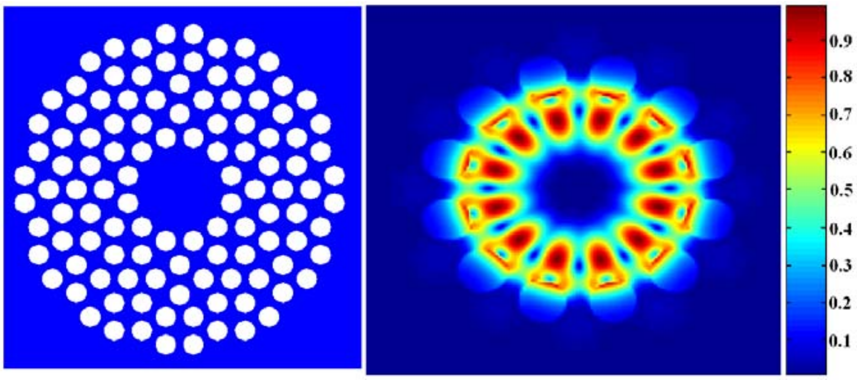

Fig. 2. 2: The simulated $WG_{6,1}$ mode in electrical field with significant zero-field distribution in 12-fold D_2 microcavity.

To find out the answer, we calculate the *Q* factor of $WG_{6,1}$ mode in 12-fold QPC D_2 microcavity with different post size. The simulation settings and scheme of 12-fold QPC D_2 microcavity membrane structure are shown in Fig. 2. 3. The lattice constant, *r/a* ratio, and membrane thickness are set to be 550 nm, 0.38, and 220 nm.

At first, we calculate the *Q* factor of $WG_{6,1}$ mode with different post diameters (*d*), which are set to be 440, 660, 880, 1100, and 1320 nm. The calculation method of *Q* factor is employing decay rate of photons in the cavity and the *Q* factor extraction equation is *Q* =

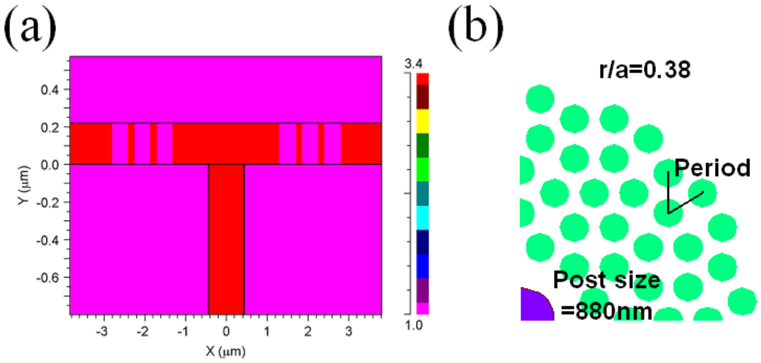

Fig. 2. 3: The scheme of 12-fold QPC D_2 microcavity with central post, including its (a) index profile and (b) lattice parameters setting.

$2\pi f \cdot \tau$. The f and τ is the frequency of WG$_{6,\,1}$ mode and the photon decay time, respectively. The calculated result of Q factor variation is shown in Fig. 2. 4. The Q factor is not degraded significantly until the d is larger than 880 nm. After that, the Q factor decreases when the post size increases. When the d is as large as 1320 nm, the Q factor of WG$_{6,\,1}$ mode decreases to 7,500. Besides, the wavelength of WG$_{6,\,1}$ mode is also red shifted when the post size increases. The wavelength is varied from 1.58 to 1.64 μm as shown in Fig. 2. 4. In fact, the wavelength dramatically changed only when d is too larger (> 880 nm), which indicates the WG$_{6,\,1}$ mode is affected by significant effective index change.

In addition, we also show the simulated WG$_{6,\,1}$ mode profiles in x-z and y-z plane when the d = 0, 880, and 1320 nm, as shown in Fig. 2. 5. From the x-z plane mode profile, one can

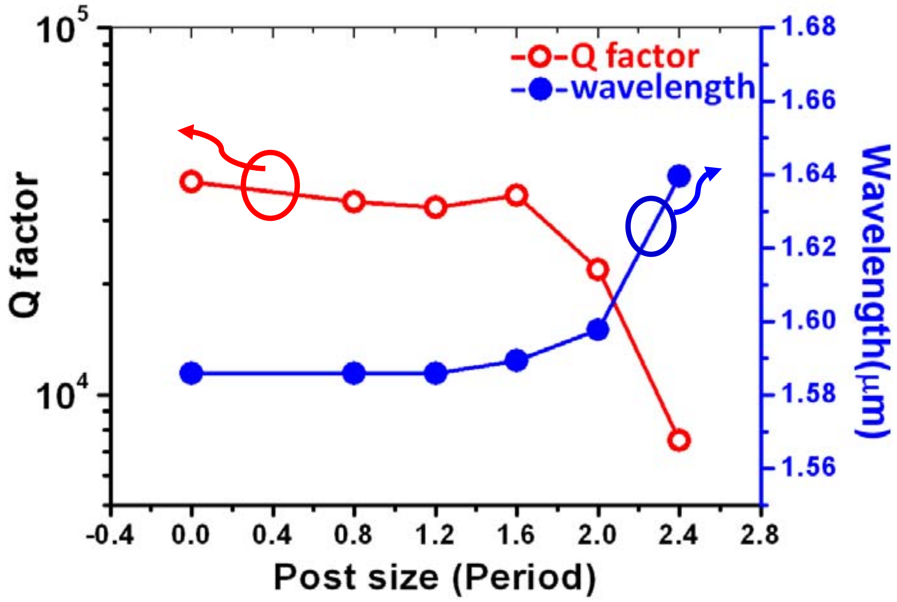

Fig. 2. 4: The Q factor and wavelength variation of WG$_{6,\,1}$ mode in 12-fold D$_2$ microcavity with different central post size. The Q factor and wavelength of WG$_{6,\,1}$ mode significantly decreases and increases when the post size is larger than 880 nm. We can confirm that WG$_{6,\,1}$ mode will not be affected by central post until its size is larger than 880 nm.

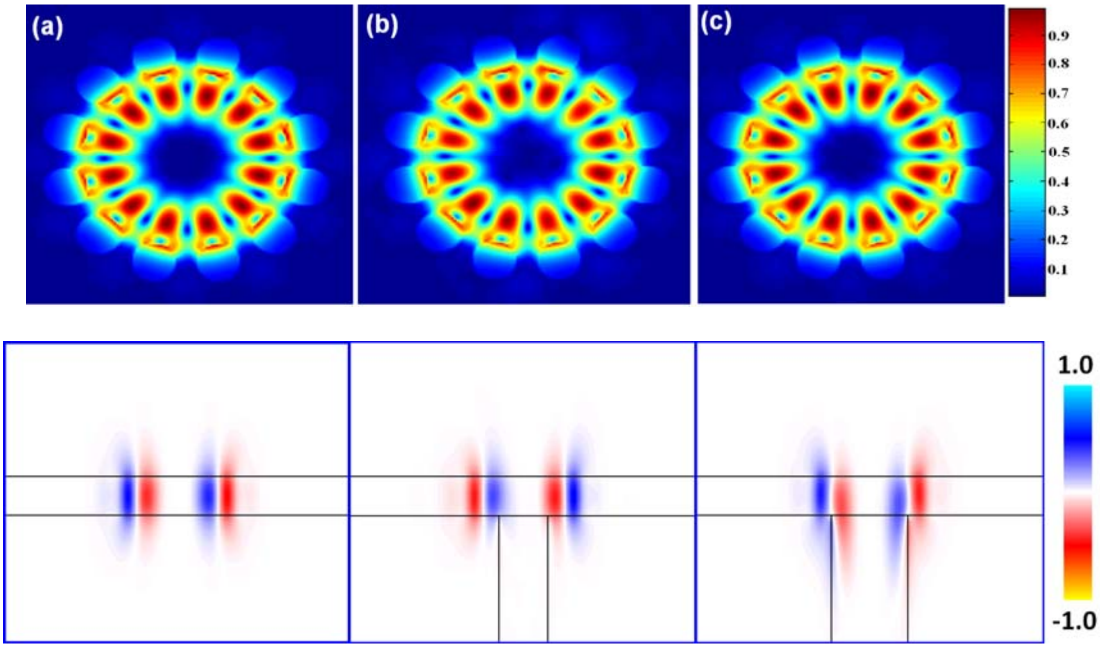

Fig. 2 .5: The simulated $WG_{6,\,1}$ mode profiles in x-z (top) and y-z plane (bottom) when the *d* is (a) 0 (membrane), (b) 880, and (c) 1320 nm.

observe the significant mode distortion when d is larger than 880 nm. From the y-z plane mode profile, one can also observe that the most energy flow of $WG_{6,\,1}$ mode loss through the central post as shown in Fig. 2. 5. From above simulations, we can confirm that $WG_{6,\,1}$ mode will not be affected until the *d* is larger than 880 nm.

2.3. Calculation of Thermal Dissipation with Different Post Sizes by Finite Element Method

2.3.1. Finite Element Method

The finite element method (FEM) is proposal by Richard Courant (1942). It can solve the boundary value problem and eigen-value problem. Most people solve the Maxwell's equation by FEM in electro-magnetical field. They divide the simulation domain into many sub-domains and substitute into equation to solve the problem. Any physics phenomenon is to a stable state. Thus, when we want to calculate a steady state of a physics problem F, we let $\delta F = 0$ by variation principle. FEM is employing the method to solve the steady state in the system.

For a boundary value problem:

$$L\varphi = f \tag{6}$$

L and φ is a self-adjoint operator and function of answer. We will divide simulation domain into many sub-domains. The sub-domains scheme is shown in Fig. 2. 6. Each sub-domain is called a element. Each element boundary is a node. We expand a element by a basis function.

$$\tilde{\varphi}^e = \sum_{j=1}^{n} N_j^e \varphi_j^e \tag{7}$$

$\tilde{\varphi}^e$ and ~ mean element and approximate solution of function φ. N_j^e means a basis function with jth node of eth element. N_j^e should be zero in another element. We can calculate the approximate solution in the simulation domain by the method.

$$\tilde{\varphi} = \sum_{e=1}^{M} \sum_{j=1}^{n} N_j^e \varphi_j^e \tag{8}$$

We substitute formula (8) into (6) to calculate and employ the variation to get the function of $\tilde{\varphi}$. M is the number of element.

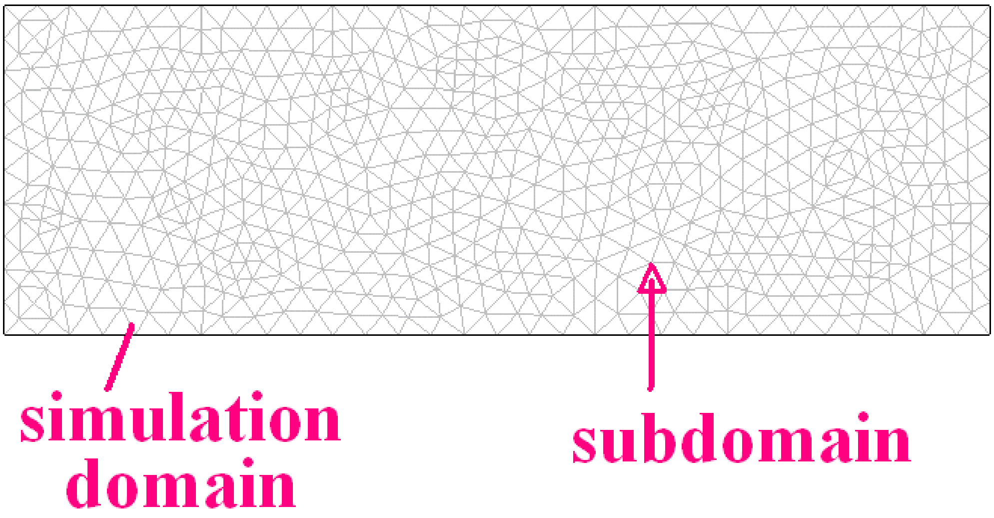

Fig. 2. 6: The illustration of domain and sub-domain definitions in FEM simulations.

We substitute formula (8) into (6) to calculate and employ the variation to get the function of $\tilde{\varphi}$. M is the number of element.

2.3.2. Heat Sink Transition with Different Post Sizes

As mentioned at last section, when the post size is smaller than 880 nm in diameter, $WG_{6,1}$ mode will be not significantly affected by the post. Besides, the thermal conductivity of InGaAsP is much higher than that of the air. Instinctively, we can treat the central post as a good heat sinker. We calculate heat dissipation of different post size of 12-fold QPC D_2 microcavity by FEM simulation. The general heat transfer equation we use in the simulation is listed in (1), where ρ, C_p, T, k, and H are denote the density of material, heat capacity of material, temperature, thermal conductivity of material, and the given heat sources, respectively.

$$\rho C_p \frac{\partial T}{\partial t} + \nabla \cdot (-k \nabla T) = H \tag{9}$$

In this thesis, we only calculate thermal conductivity without convection and radiation. Because we find that the convections and radiations are relative small compared with the conductions, thus, we will ignore the temperature variation caused by the convections and radiations in our simulations.

The 12-fold QPC D_2 microcavity shown in Fig. 2. 3 is also setup in the FEM simulations. The lattice constant, r/a ratio, and slab thickness are set to be 550 nm, 0.38, and 220 nm respectively. The simulation domain is a circle with 11 μm radius in x-y plane and the air cladding thickness in z-direction is set to be 2 μm. Besides, due to the symmetry benefit of the QPC lattice structure, we use an one-six reduced domain in the simulation in order to save computer memory and simulation time consumption, as shown in Fig. 2. 7. We also list the materials parameters we used in simulations in Table I.

Fig. 2. 7: Scheme of one-six domain of 12-fold QPC D_2 microcavity in the FEM simulation setup. The air-cladding thickness, lattice constant, *r/a* ratio, and slab thickness are set to be 2 μm, 550 nm, 0.38, and 220 nm, respectively.

Table I: The used material parameters in the simulations.

	k (Thermal Conductivity) (W/m・K)	**ρ(Density) (kg/m^3)**	**C_p(Heat Capacity) (J/kg・K)**
Air	**1.205**	**1.025**	**1006**
InGaAsP	**39.871**	**5445.16**	**282.26**
Sapphire	**35**	**3965**	**730**

The main heat in the microcavity is generated by the carrier non-radiation recombination due to the pumped laser energy at the surface. In the simulation, we regard the pumped laser as an electro-magnetic wave and the total electro-magnetic wave energy is transferred to heat, that is, the worst case. We subtract the components of reflection of pumped laser due to light propagation from low to high index, which is estimated as 30%. The remaining pumped laser energy is totally transferred to heat. Thus, the assumptive heat sources are smaller than the real power pumped on the microcavity.

Generally, the pumped laser energy is several milli-watts and the emission from multi-quantum-wells (MQWs) is hundred of nano-watts. Thus, the large temperature raise is mainly caused by the former one rather than the latter one. In our simulation setup, this relative small optical emission component is ignored. The heat source is given by the command listed in (2). The term A of command (2) denotes the region of heat sources, in this case, a circular region with radius of 0.8 μm. The term B is the duration time of the heat source, in this case, a pulse with 25 ns. And the C term is heat energy that is calculated by the equation (3), where W, S and E is pumping energy, pumping area and energy per m^3. The term D means that the electro-magnetic wave transmits to the dielectric material and is absorbed by the material, that is, the energy skin depth related to the absorption coefficient of the material α (for InP, $\alpha = 3.5\times10^6$). Besides, the position of the heat source is also given in term D, in this case, at the surface.

$$\underset{\mathbf{A}}{\underline{\mathbf{(x^2+y^2)^{0.5}<8.02\cdot10^{-7}}}}\cdot\underset{\mathbf{B}}{\underline{\mathbf{(t<25\cdot10^{-9})}}}\cdot\underset{\mathbf{C}}{\underline{\mathbf{E}}}\cdot\underset{\mathbf{D}}{\underline{\mathbf{exp(-3.5\cdot10^{6})\cdot(2.2\cdot10^{-7}-z)}}} \qquad (10)$$

$$\frac{W}{\pi\cdot S}\cdot\alpha = E \qquad (11)$$

$$\mathop{\oiint}\limits_{\mathbf{s}}\mathbf{\vec{F}\cdot\hat{n}dA} = \mathop{\iiint}\limits_{\mathbf{v}}\mathbf{(\nabla\cdot\vec{F})d\tau} \qquad (12)$$

In the simulation, the Gaussian formula will be employed to the calculation shown in equation (12). The heat source term will be adapted into the equation (9). And then this term will be multiplied to equation (10). The boundaries conditions we set are thermal insulation and axial symmetric. The thermal insulation means that the quantity of in- and out-ward heat sources passing equally through the surface. If we set the boundary condition that is equal to 300k, the boundary will be treated as the cooling source. In our simulation setup, the top,

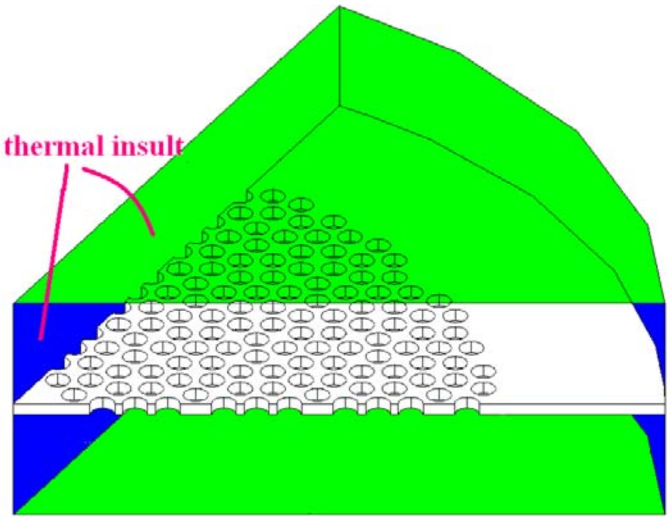

Fig. 2. 8: Scheme of the boundary settings in the simulation.

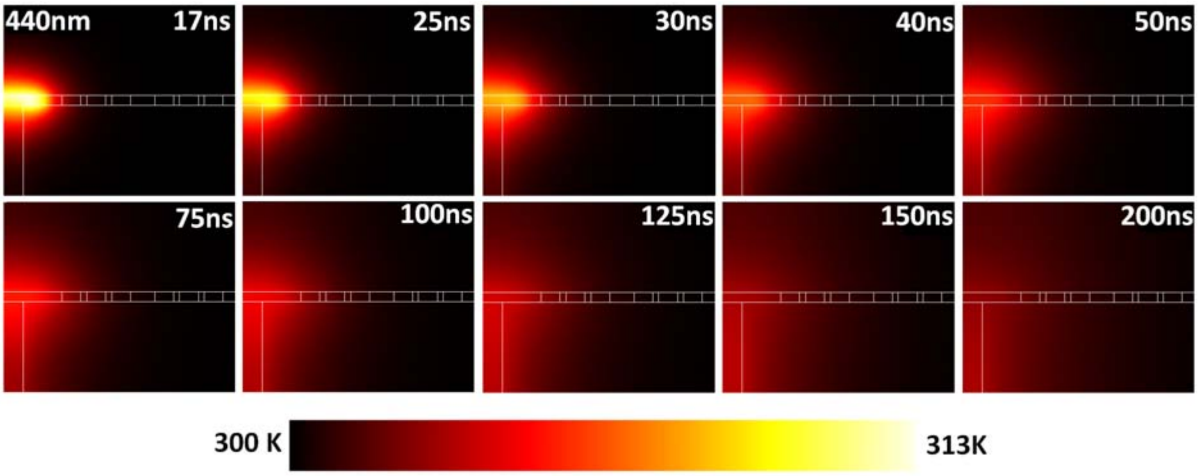

Fig. 2. 9: The simulated temperature distribution in y-z plane of 12-fold D_2 microcavity with central post *d* = 440 nm. We can confirm that heat is loss to the central post. The highest temperature is 310.1 K on 17 ns. The decay rate of temperature is 53.8 ns.

bottom, and the back boundaries are set to be thermal insulation. And the side boundaries are set to be axial symmetric, as shown in Fig. 2. 8. The simulation time is set to be 400 ns, which is limited by our computer capability.

First, we want to confirm that the central post can really play the role of heat flow pathway in our assumption. We calculate the heat transition behavior by inserting a 440 nm central post under the 12-fold QPC D_2 microcavity. The pumped laser energy and its pulse duration are set to be 2 mW and 25 ns, respectively. And the simulated temperature distributions when t = 17 to 200 ns are shown in Fig. 2. 9. In Fig. 2. 9, we can easily find that the heat energy is loss from the cavity through the central post. The highest temperature in this case with central post is lower than that in the membrane structure. That means the heat dissipation of central post structure is could be better than that of membrane structure.

From above results, instinctively, is there better heat sinking with larger central post? To confirm this assumption, we further simulate the heat sinking behaviors of 12-fold QPC D_2 microcavity with different central post sizes of 440, 660, and 880 nm in diameter. The

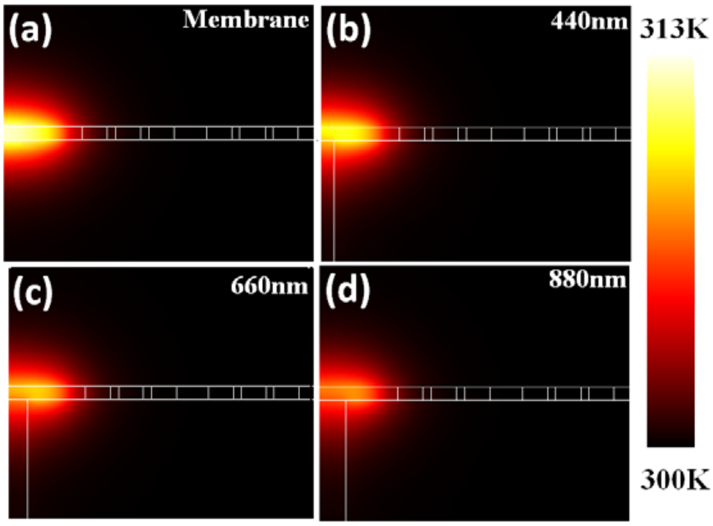

Fig. 2. 10: The simulated highest temperatures in the case of (a) membrane, (b) 440, (c) 660, and (d) 880 nm central posts under the microcavity. It is obviously that there will be better heat sinking effect when the post size is 880 nm in diameter.

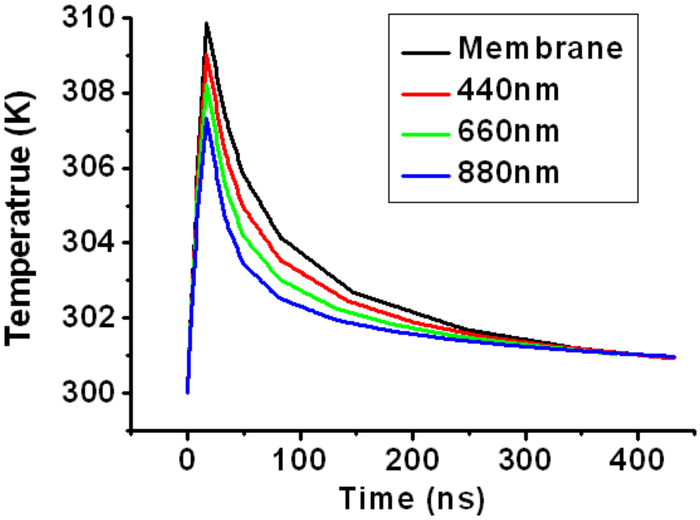

Fig. 2. 11: The simulated temperature decay curves with different central post sizes.

simulated highest temperatures of membrane, 440, 660, and 880 nm central post under the microcavity are 312.3, 310.1, 308.9, and 307.7K, respectively. Their temperature distributions are also shown in Fig. 2. 10. From these results, it is obviously to observe that the heat sinking will be better when the post size is getting larger. Besides, we also find that there will be faster cooling rate for larger post case. The cooling rate is defined as the time of temperature degraded to 1/e. In the temperature curves shown in Fig. 2. 11, the cooling rate of membrane structure, 440, 660, and 880 nm posts are 53.8, 42.0, 37.0, and 31.5 ns, respectively.

As we mentioned before, the poor heat sink of the air-cladding in membrane structure has long been regarded as a huge obstacle in achieving CW lasing action. Thus, for a high *Q* mode, under the assumption that the other factors can be ignored, we can claim that the CW lasing can be achieved if the heat sink can be further improved. To judge the heat sink is improved or not, we have to refer the thermal properties of low *Q* mode in photonic crystal D_3 microcavity in our previous researches [15]. In our previous works, the low *Q* mode does not lasing until the substrate temperature is increased to 323 K. In our previous simulation, the

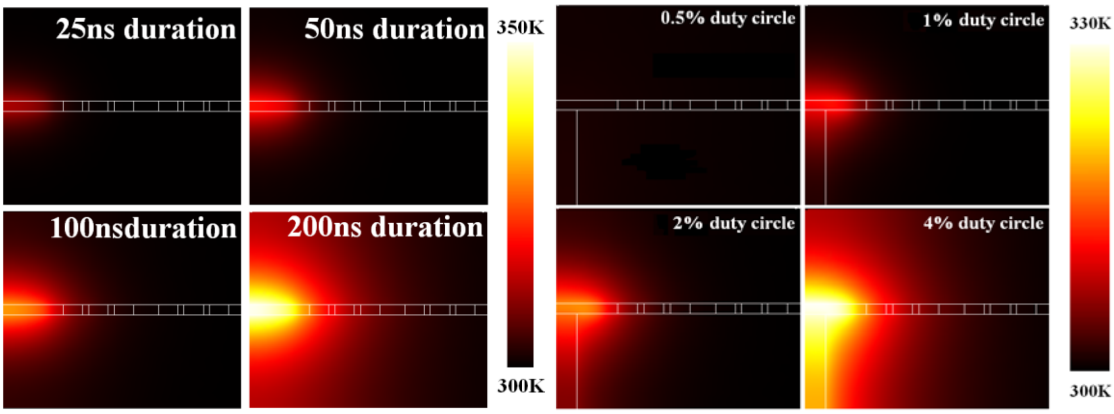

Fig. 2. 12: The highest temperature of the membrane structure is 343 K when the pulse duration is 200 ns. And the highest temperature of 880 nm central post size reaches 343 K when the pulse duration is 300 ns.

temperature will be 12 K higher than the room temperature (300K). Thus, by combining these two information, we can assume that the CW lasing could be achieved when the highest temperature of the microcavity decreases to 335 K. It is also necessary to note again that the situation we assume here is the worst case.

And then, we want to know how large energy can be received in different central post sizes. Thus, we set the heat source with different pulse duration of 25, 50, 100, 200, and 300 ns. The simulated results are shown in Fig. 2. 12. The highest temperature of the membrane structure is 343 K when the pulse duration is 200 ns. And the highest temperature of 880 nm central post size reaches 343 K when the pulse duration is 300 ns. The improved Heat dissipation of 880nm central post size is better than air-cladding structure. In addition, we also calculate the widely-used electrically-driven structure in microdisk by inserting top and bottom posts as shown in Fig. 2. 13. The simulated highest temperature is also lower in the 880 nm post case than that in membrane structure.

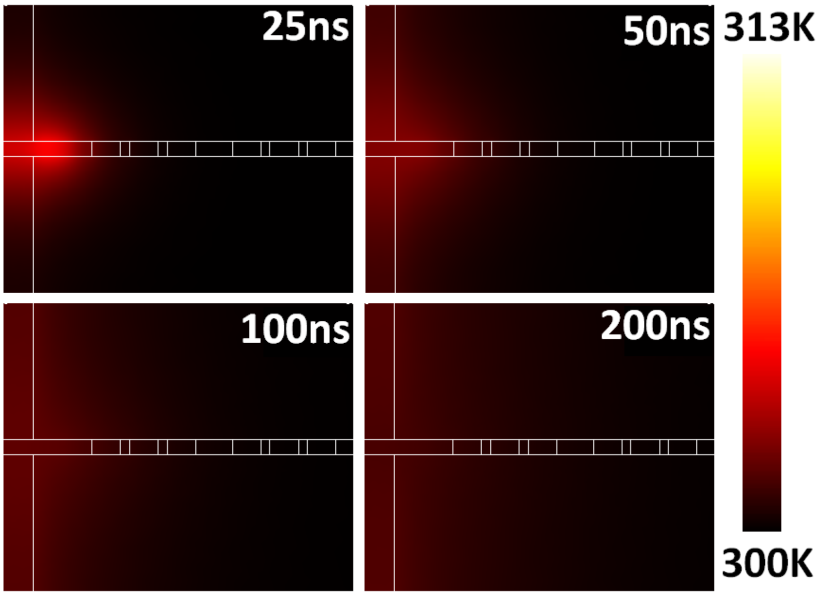

Fig. 2. 13: The simulated highest temperature of 12-fold microcavity with top and bottom post size of 880 nm under different pump laser pulse duration of 25, 50, 100, and 200 ns.

Actually, in our fabricated 12-fold QPC D_2 membrane microcavity, the measured threshold is only about 280 μW. And according to our previous simulations and measurements, if the $WG_{6,1}$ mode is not affected by central post, the threshold will not raise significantly. That means it does not need so large power (in our simulations, 2 mW) to excite the microcavity.

The simulated highest temperature and *Q* factor of $WG_{6,1}$ mode with different post sizes is shown in Fig. 2. 14. When the post size is larger than 880 nm, *Q* factor is degraded and the heat sink is improved. If we request good heat sinking, it will sacrifice *Q* factor and threshold of $WG_{6,1}$ mode. That means there is a trade-off between the heat sink and *Q* factor in this post structure. When the post is larger than 880 nm, it can be expected that the threshold will

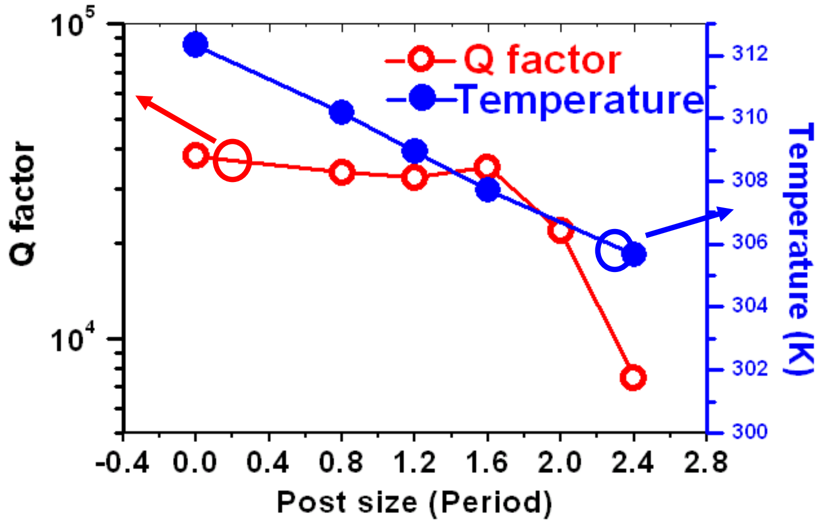

Fig. 2. 14: The simulated highest temperature and *Q* factor of $WG_{6,1}$ mode of 12-fold QPC D_2 microcavity with different post sizes.

become larger and need more energy to lasing. At the same time, the high pumping energy will produce more heat and leads to a vicious circle. Thus, it is necessary to find a balance when considering *Q* factor and heat sink. From our simulated results, the post size of 880 nm would be a good choice and potential to achieve CW lasing actions.

2.4. Comparison with Sapphire-Bonded Structure

As we mentioned above, the continuous-wave (CW) lasing operation of photonic crystal microcavity has long been a big challenge, which is mainly limited by the poor heat sink of the air-cladding in membrane structure. Very recently, there are several reports of photonic crystal micro- and nanocavity (cavity size < 3 μm in diameter) CW lasing, including L_3 [16] and D_0 (point-shifted) [17] nanocavity with air-cladding, D_4 microcavity with sapphire substrate [18], and D_1 nanocavity with fluidics [19]. In former two and latter two cases, spontaneous emission control and improved heat sink are used in order to achieve CW operations. However, all of them are still leaking of a promising electrical driving structure which are limited by their mode profiles or asymmetry structure. By combining the electrically driven structure and heat sinker based on central post we proposed above, we believe the 12-fold QPC D_2 microcavity with large central post can provide a promising approach for electrically-driven CW operated photonic crystal microcavity lasers.

In this section, we would like to take the sapphire-bonded D_4 photonic crystal microcavity for comparison with our structure. In the sapphire-bonded structure, the sapphire is only bonded in one side and forms an asymmetric structure. The simulated results of sapphire-bonded structure under pump energy with 25ns pulse durations are shown in Fig. 2. 15. In the scheme, the heat dissipation is better than membrane and central post structure. The highest temperature of sapphire-bonded structure is lower 7 and 5 K than membrane structure and 880 nm central post as shown in Fig. 2. 16, which shows very good heat sink effect.

However, there is a big problem in sapphire-bonded structure. Because the refractive index of sapphire is 1.6, the index difference between air and sapphire form a asymmetric structure and induce extra optical losses for the microcavity. We calculate $WG_{6,1}$ mode profile of 12-fold QPC D_2 microcavity in sapphire bonding structure by 3D FDTD as shown in Fig. 2. 17. And we also calculate its *Q* factor by photon decay fitting. The *Q* factor of $WG_{6,1}$ mode is 850, which is much lower than that of microcavity with 880 nm central post. Although the sapphire-bonded microcavity achieves better heat dissipation, the *Q* factor is greatly decreased and limits its application tolerance.

In our central post structure, if the $WG_{6,1}$ mode with high *Q* factor and lower threshold could be operated at low-energy excitation, the heat generated and the increased temperature by the pumped laser will not be terrible as in our prediction in simulations. Thus, we believe the 12-fold QPC D_2 microcavity with proper central post size is very potential in achieving electrically-driven CW lasing actions.

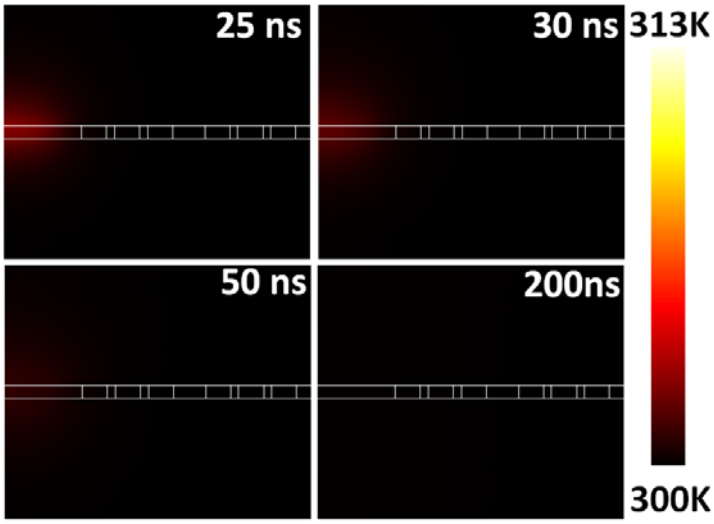

Fig. 2. 15: The simulated highest temperature of sapphire-bonded structure under pump energy with different pulse durations from 25 to 200 ns.

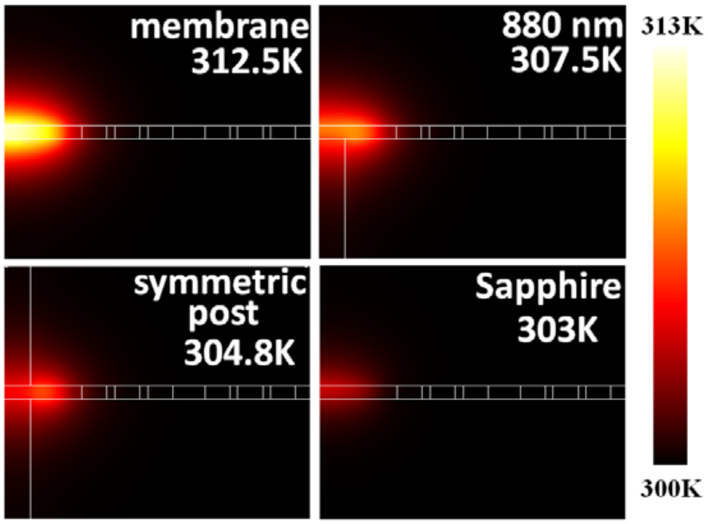

Fig. 2. 16: The simulated highest temperature of membrane, 880 nm asymmetric, symmetric post, and sapphire-bonded structure under the pumped laser energy with 25 ns pulse duration.

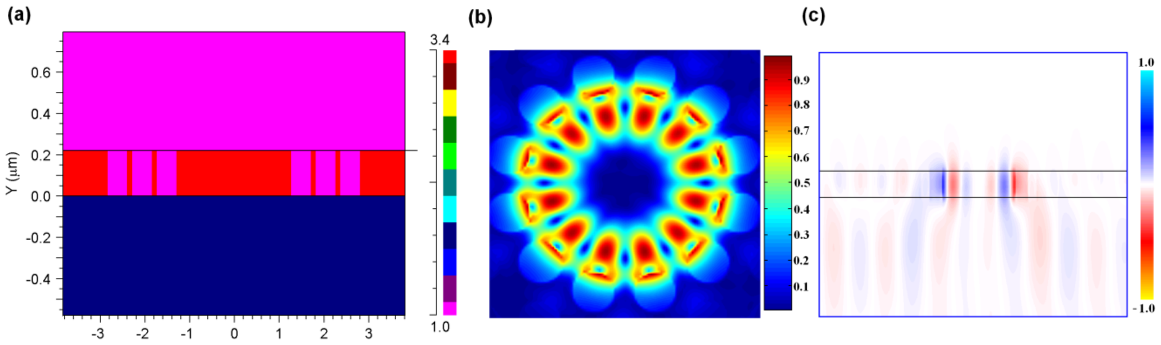

Fig. 2. 17: (a) The 3D FDTD simulation setup of sapphire-bonded 12-fold QPC microcavity, (b) the simulated $WG_{6,1}$ mode profile in electric-filed and (c) the simulated $WG_{6,1}$ mode profile in vertical direction.

2.5. Conclusion

In this chapter, at first, we investigate the influence on *Q* factor of $WG_{6,1}$ mode caused by the induced central post by 3D FDTD simulation. We find that there will be no significant influence on *Q* factor when the post size that is smaller than 880 nm in diameter, which are confirmed by *Q* factor degradation and wavelength red shift. In this case, the simulated *Q* is still as high as 38000. And then we further investigate the heat sink effect caused by the central post by FEM simulations. From the simulated results, we can summarize that heat sink with central post is better than that of membrane structure. Besides, we can conclude that there is a trade-off between the *Q* factor and the heat sink improvement. The post size of 880 nm in diameter will be the proper choice.

We also take the sapphire-bonded structure with CW lasing for comparison. Although the heat sink of sapphire bonding structure is better than others, the *Q* factor of its much lower than the central post structure due to the asymmetric structure. Thus, if the *Q* factor of $WG_{6,1}$ mode in microcavity with is sufficient high, the necessary pumping energy will be small and the heat generated by pumping energy will be also smaller than we predict in the simulation. Thus, we believe the 12-fold QPC D_2 microcavity with central post size of 880 nm in diameter is very potential in achieving electrically-driven CW lasing actions with large application tolerance.

Chapter 3 Electrically-Driven Structure

3.1. Introduction

In this chapter, we focus our researches on the fabrication process of mesa for electrically driving and the electro-luminescence (EL) measurement system. At first, we will fabricate the mesa for electrically-driven photonic crystal microcavity laser. In the developed fabrication processes, photo mask design, disk-type mesa formation, related dry-etching technology, and electrode design will be investigated. And then the photonic crystal membrane microcvity with central post will be fabricated on this mesa. Besides, we also setup a micro-electro-luminescence system, which can be used for examine the degradation of MQWs during the mesa fabrication processes.

3.2. Wafer Structure

In order to achieve electrically diving, our wafer epitaxial structure is doped, which is different from that of membrane structure. The electric resist can be reduced in the wafer with dopant. In the doped epitaxial structure, we can get larger emission power of QW by smaller driving voltage. Our designed epitaxial structure is shown in Fig. 3. 1. The wafer epitaxial structure that we design is n-i-p structure. The n-i-p structure has an advantage for our investigation. This is because that the central post is the electric conductivity path in our structure. And we hope that the emission region of QW is localized in microcavity. And the drift velocity of holes is much slower than that of electron. When the holes pass through the central post to cavity region, the holes will be trapped without leaving the microcavity region. Holes and electron will recombine and produce light in the microcavity region. If we use the

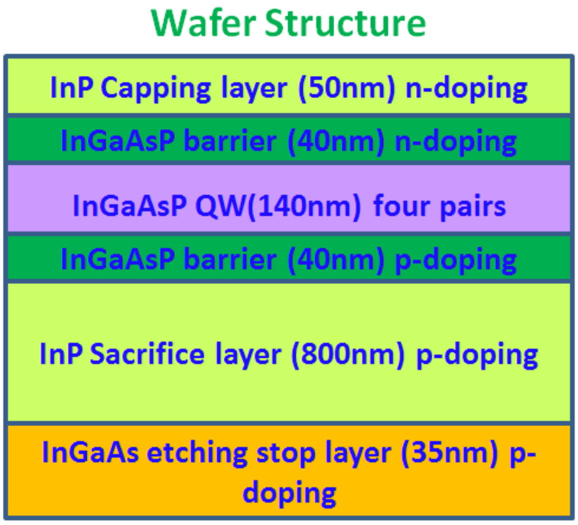

Fig. 3. 1: The epitaxial structure of doped InGaAsP MQWs for electrical driving by central post.

p-i-n structure, the recombination region will not concentrate on the microcavity. The injection and emission efficiency will be very poor. We add a stop etching layer in our structure. When we fabricate the mesa, the undercut by wet etching will stop at this layer. The wet etching of InP is anisotropic. If there is no stop etching layer in the structure, the mesa will be unstable and the central post size will be non-uniform after wet etching.

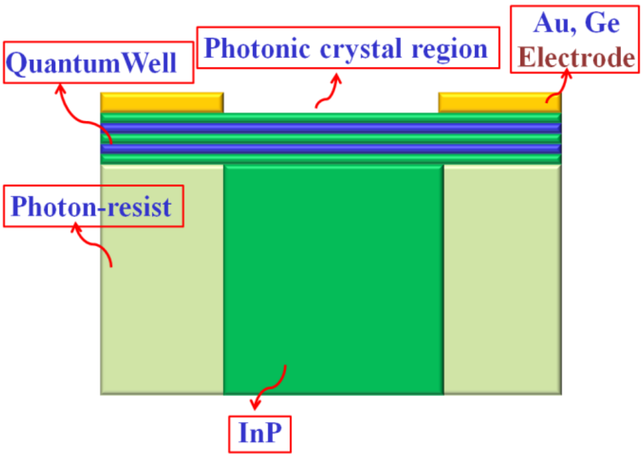

Fig. 3. 2: The scheme of mesa structure for electrically-driven photonic microcavity lasers

3.3. Mesa Fabrication

The scheme of mesa for electrical driving we design is shown in Fig. 3. 2. We can divide our fabrication to four steps. All processes of mesa fabrication are shown in Fig. 3. 3.

First, we will define the patterns of mesa. We employ the photolithography to define the mesa pattern and then it will be transferred into the InP layer by ICP dry etching process, as shown in step A in Fig. 3. 3. Second, the sacrificed layer under the MQWs layer will be etched by diluted HCl selective wet-etching process. And the disk structure will be formed, as shown in step B in Fig. 3. 3. The etched undercut width will be the same as the width of electrode. Third, the etched undercut will be filled with photon-resist (PR). This is because we

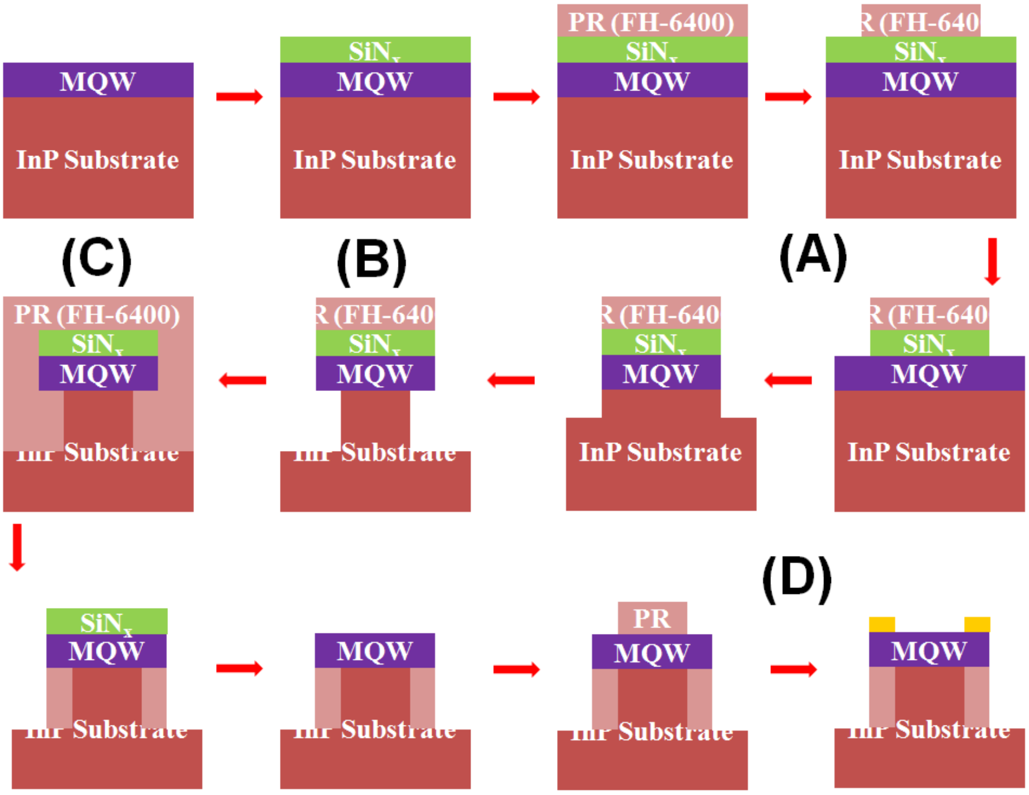

Fig. 3. 3: The overview of fabrication process of mesa.

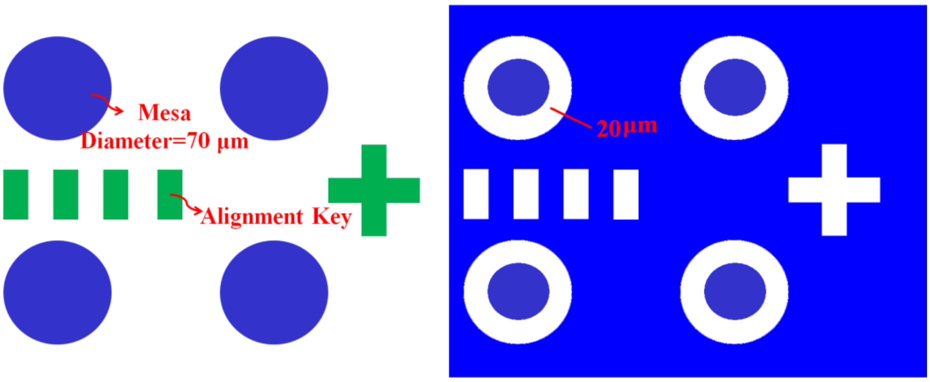

Fig. 3. 4: Photo mask design of mesa and electrode.

do not want any current pathway except central post. Besides, the MQWs layer will be also sustained by the filled PR layer. The PR structure should be harden and sustain the MQWs layer after deposited electrode process. Forth, we employ the photolithography to define the pattern of electrode and deposit it on mesa by thermal coater.

3.3.1. Photolithography and ICP Etching

At first, we will deposit SiN served as hard mask on the InP layer. And then we define the mesa pattern by using photolithography process. We design three different mesa sizes of 70, 90, and 110 μm, respectively. The large mesa can avoid probing trouble in EL measurement due to smaller electrode. It is difficult to contact the smaller electrode by the probe size of 5 μm. Our mesa mask pattern is shown in Fig. 3. 4. The distance between mesas is 200 μm. The alignment keys of mask we design are four rectangular and a cross shape between mesas in transverse and longitudinally direction. We can align by alignment key easily in first and second lithography.

The PR that we use is FH-6400. The parameters of PR spinning are first step the rotation rate of 1,000 rev / sec and second step the rotation rate of 4,000 rev / sec. The thickness of the

PR in this recipe is about 1.6 μm. The MQWs can resist the Van del Waal's Force and avoid the collapse of MQWs by the PR layer. The thickness of PR can hold the MQWs membrane without collapsing. The exposure and develop time in this recipe are 30 and 60 seconds. The developing dilute is FHD-5. Subsequently, we will etch the SiN and InP by ICP-RIE. We will transfer the patterns of mesas to SiN without cleaning PR. And then transferring patterns to QW and InP. The etching of InP recipe should be as short as possible or it will destroy the structure of the PR. The mesa patterns can be fabricated by this recipe.

3.3.2. Undercut First Time

After we defined the patterns of mesas, we will form the undercut under the MQWs which is prepared for the following PR filling. The most of currents will only pass through the large central post in this design when we apply the electrical source. Due to the large etched region, fast etching rate is needed. Thus, the HCl : H_2O is 3 : 1 at room temperature instead of 2°C used in general photonic crystal microcavity fabrications. The etching rate of this recipe is about 10 μm / min and the wet-etching time is about two minutes. And we do not use the magnetic rotator to fasten the etching rate, because the suspended MQW layer is too fragile. Originally, if we clear the PR after ICP dry-etching, the MQWs will collapse after undercut due to Van del Watt's force. The collapse mesa is shown in Fig. 3. 5. Thus, we do not clear the PR before re-filling the undercut with PR. Because the InGaAsP material is so soft, the thin MQWs layer will easily collapse. Therefore, we can employ the hardened PR to hold the MQWs. The sample direction should be vertical when clipping sample in the HCl dilute. The mesa is shown in Fig. 3. 6 after undercut wet-etching.

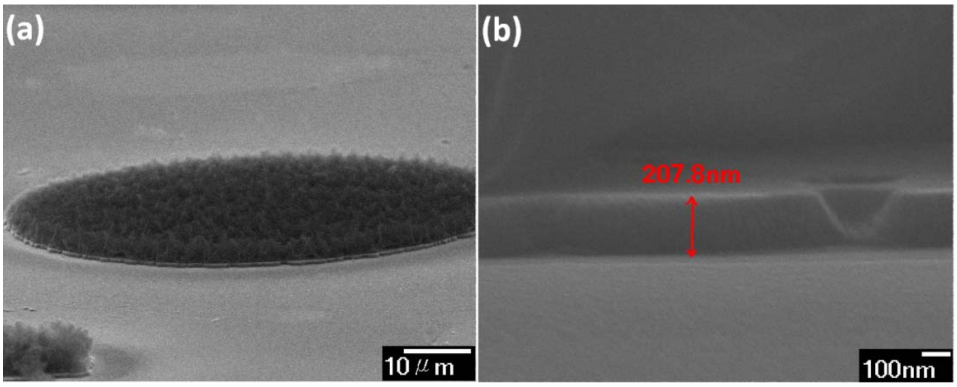

Fig. 3. 5: The (a) tilted and (b) cross-section SEM of the failed sample after wet-etching undercut by HCl solution.

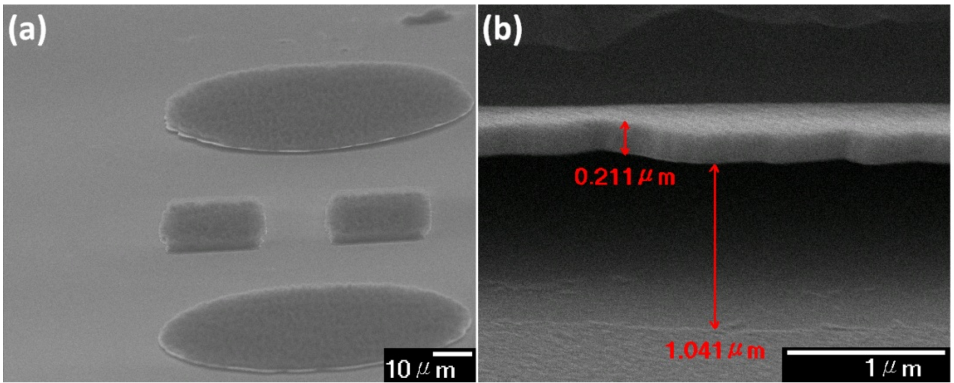

Fig. 3. 6: The tilted (left) and cross-section (right) SEM of the suspended membrane in air after wet-etching undercut by HCl solution.

3.3.3. *Fill with PR and Clean SiN and PR*

After wet-etching by HCl diluted, we should fill undercut by PR as soon as possible. The suspended MQWs layer will collapse due to the gravity force or any shocks. The PR FH6400 is filled in the undercut by spin coater. The recipe is the same as photolithography we used in last paragraph, but the spin time of second step is shortened to 5 seconds. And then the PR will be consolidation by hot plate at 120°C. After hard bake the PR, we can check that MQWs layer collapses or not by optical microscope first. The failed situation is shown in Fig. 3. 7 (a).

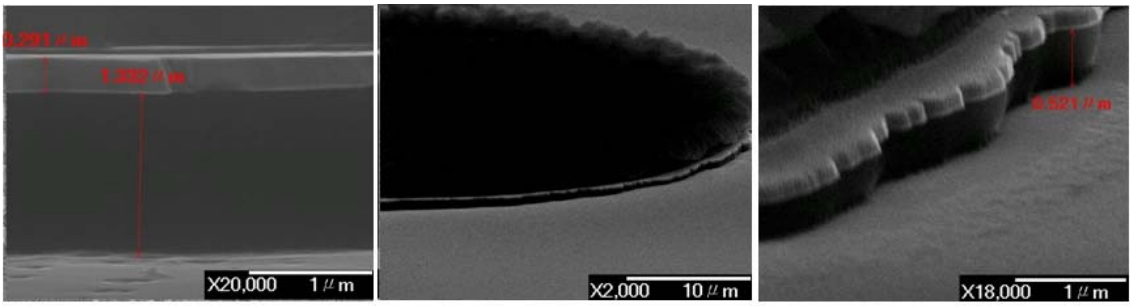

Fig. 3. 7: The SEM pictures of undercut filling with PR.

When the post boundary shows the black color, it means that the MQWs layer has collapsed. In Fig. 3. 7 (b), we can find that the altitudes of the post and another position. Then we will clear the PR by O_2 plasma and remove SiN_x by BOE wet-etching process. We can also remove the residue PR by cleaning SiN_x.

The SEM pictures of undercut filled with PR are shown in Fig. 3. 8. The SEM pictures of cleaning SiN and PR are shown in Fig. 3. 8. The boundary of the post is not uniform, because the PR is shrunk after hard bake. Once the MQW layer is not broken, the injected current should not be affected.

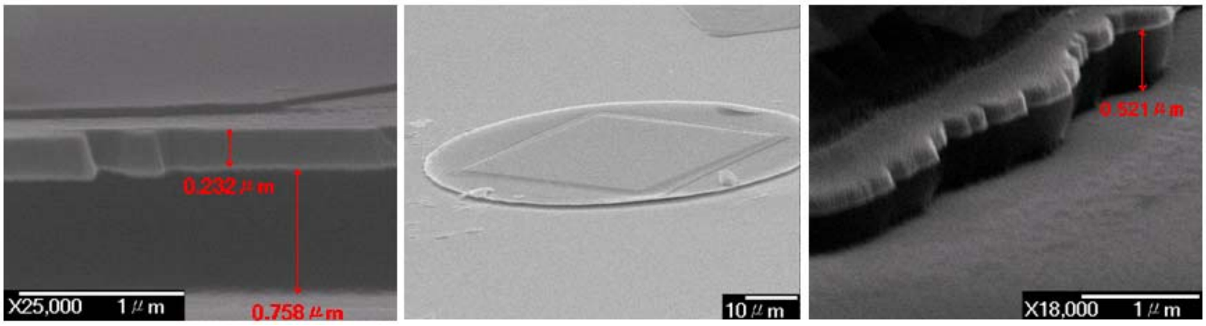

Fig. 3. 8: The SEM pictures of mesa with PR-filled undercut after cleaning PR and SiNx residue by O_2 plasma and BOE wet-etching.

Finally, we will further hard bake the PR at 250°C to make sure that it will not be dissolved by Acetone solution in the following fabrication process. We will confirm that there are PR and SiN_x residue at MQWs surface or not by PL measurement. The measured PL spectrum is shown in Fig. 3. 9. We can find that the PL spectrum with free spectral resonance, which could be caused by Fabry-Perot Effect. Thus, we calculate the Fabry Perot effect by the equation (1). The effect is from the large InP post region under the MQWs. The wavelength λ_0 and refractive index n are set to be 1.55 μm and 3.4, respectively. The L is the post region size and is calculated as 35 μm.

$$\Delta\lambda = \frac{\lambda_0^2}{2 \times n \times L} \qquad (1)$$

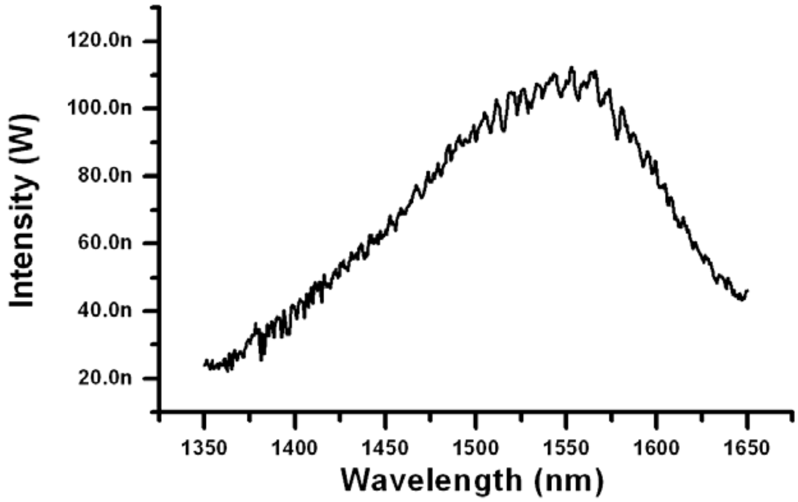

Fig. 3. 9: The measured PL spectrum from mesa with PR-filled undercut. The free spectrum resonance is caused by Fabry-Perot Effect.

3.3.4. Deposit Electrode

In the last step, we will deposit the electrode on the mesa for electrically pumped. The spinning on PR and exposure recipe is the same as mention above. The second step of photolithography has some problem when aligning alignment key. And then the electrode will be evacuated by the thermal coater. The material of electrode is Au. After evacuating the electrode, the Au residue will be lifted off by acetone. Au is flaked easily without deposited Ni before Au. Thus, the lifted off time should be short. The thickness of electrode is 100 nm. The complete mesa with Au electrode is shown in Fig. 3. 10.

3.4. Electro-Luminescence Setup

In order to measure characteristic of our mesa of 12-fold QPC D_2 microcavity, a NIR micro-PL system with sub micrometer scale resolution in space and sub nanometer scale resolution in spectrum is used. The simple configuration of the micro-PL system is shown in Fig 3. 11.

In this system, the mesa is driven by the probe contact and current injected by pulse generator. The pulse generator can operate on continuous-wave and pulse. The probe is

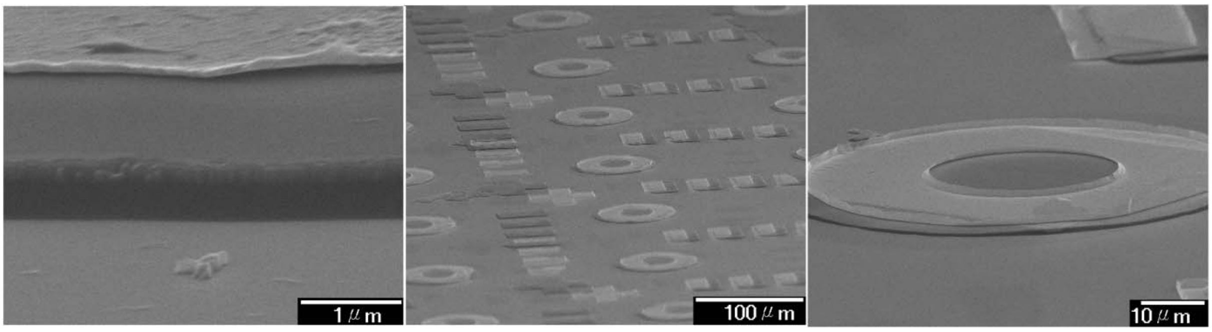

Fig. 3. 10: The SEM pictures of fabricated mesa with Au electrode.

contacted on the substrate in positive electrode and on the electrode of mesa in the negative electrode. The light emitted from the mesa is collected by the same objective lens. We use a collective lens to feed the output signal into a multi-mode fiber, and then the signal is detected by the spectrum analyzer, Ando AQ-6315A, with 0.05 nm resolution. All of the following measurement results were estimated by this micro-EL system.

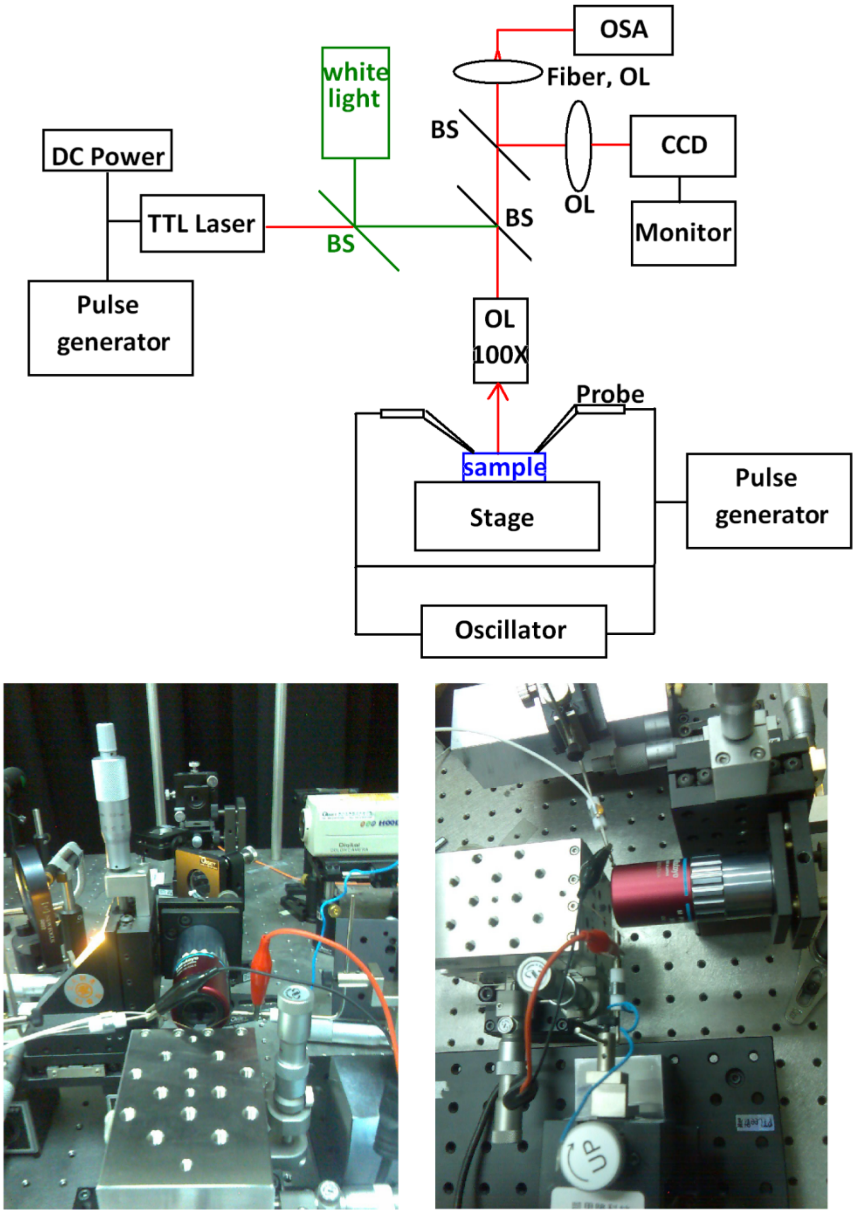

Fig. 3. 11: The illustration and pictures of micro-EL measurement system.

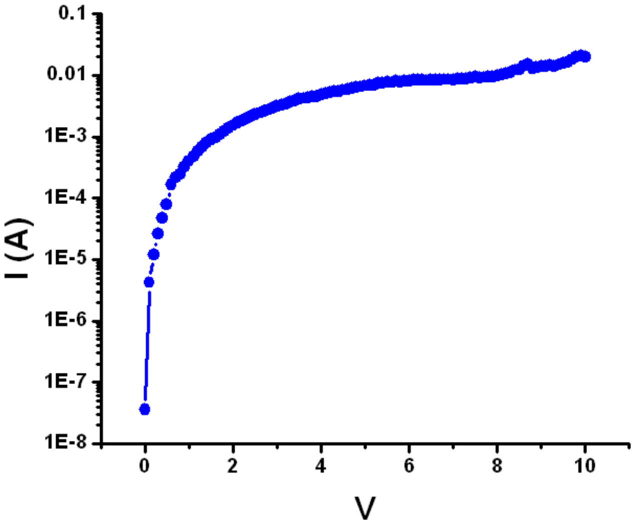

Fig. 3. 12: The measured I-V curve from mesa with contact by HP-4156B. The current can achieve 0.01 A when the voltage is 6 V.

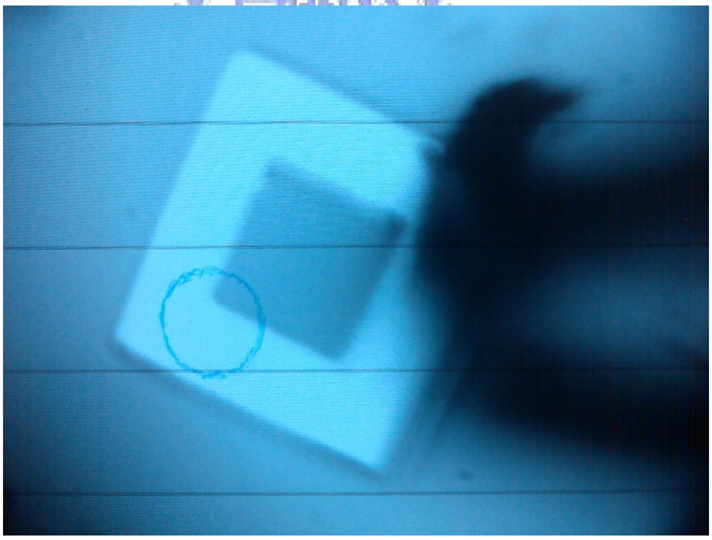

Fig. 3. 13: The picture of probing contact from CCD monitor. The white area is the Au electrode with 20 μm width. The black region is the probe.

3.5. Electro-Luminescence Measurement

After mesa fabrication, we measure the *I-V* curve of it by HP-4156B. The measured result is shown in Fig. 3.12. We can know the mesa structure that is a p-n diode from Fig. 3. 12 and we can also confirm that the Au electrode is ohmic contact. The current can achieve 0.01 amp (*A*) at 6 voltage (*V*) and the electrical resist is calculated as 800 ohms. And then we measure EL spectrum by the micro-EL system. The picture of probing contact from CCD monitor is shown in Fig. 3. 13. The result of EL spectrum measurement of the mesa is shown in Fig. 3. 14. The wavelength and intensity of emission peak from the mesa is 1524 nm and 823 nW at 5 *V*.

3.6. Conclusion

In this chapter, the mesa fabrications of 12-fold QPC microcavity are complete. We solve many issues from the fabrication process, for example, the harden PR can sustain the

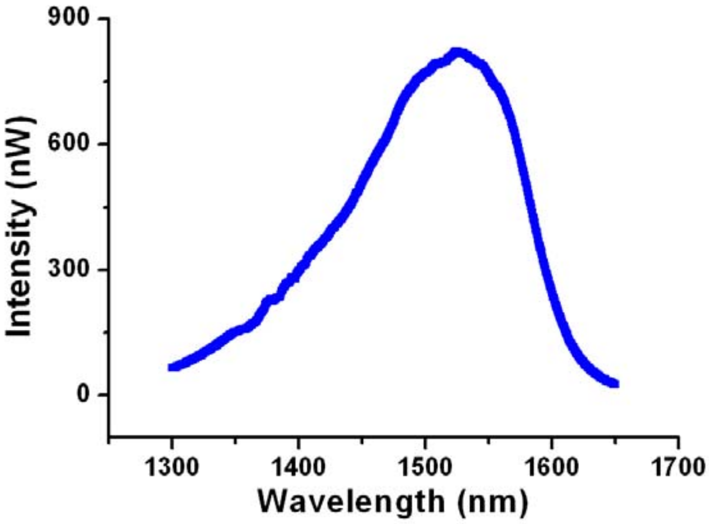

Fig. 3. 14: The measured PL emission from the mesa with electrode by micro-EL system.

fragile MQWs membrane before filling PR in undercut and finding the fabrication condition of filling the isolation region with PR. We control the post size difficultly by HCl solution. We can make sure that the PR and SiN_x is cleaned by PL measurement after cleaning SiN_x. And the emission of mesa can be measured by our micro-EL system. Finally, we can fabricate 12-fold QPC D_2 microcavity on this mesa for electrical driving.

Chapter 4 Conclusions and Future Work

4.1 Conclusions

In this thesis, we have introduced some bottlenecks of present photonic crystal in membrane microcavity in the chapter 1, mainly in electrically-driving and CW operation. In order to overcome this bottleneck, the use of 12-fold QPC D_2 microcavity with central post is presented in this thesis.

At first, by using 3D FDTD simulations, we estimate the optical loss induce by different central post size from 0 to 1320 nm from the calculated Q factors. From the simulated result, we found that there will be no significant influence on $WG_{6,1}$ modal properties (including Q factor and wavelength) when the post size is smaller than 880 nm in diameter. The simulated Q factor is 35000 when the post size is 880 nm in diameter, which is almost invariant compared with original Q factor (38000).

In addition, we also investigate extra heat sink effect provided by the post by using FEM simulation. From the simulated results, we find the heat flow will be transferred from the central post. And the simulated temperature of the microcavity will be reduced for larger central post. The temperature will reduce from 312 to 307 K when the post size is increased from 0 to 880 nm. Thus, we can conclude that the heat sink will be better for larger central post. However, this heat sink will be limited by the post size when considering Q factor. Thus, we can conclude that the post size of 880 nm ($1.6a$) will be the best choice for the trade-off between Q factor and the heat sink effect.

We also compare our structure with sapphire-bonded structure in *Q* factor and heat sink. In our simulation, although the temperature (303 K) of micrcavity is much lower than our structure, we find that the *Q* factor of our structure (38,000) is much larger than sapphire-bonded structure (850). The microcavity with lower *Q* factor leads to higher threshold and needs more pump energy to achieve lasing. Therefore, we do not sacrifice the *Q* factor and increase threshold power to produce more heat. Thus, we believe the 12-fold QPC D_2 microcavity with central post size of 880 nm in diameter is very potential in achieving electrically-driven CW lasing actions with large design and fabrication tolerance.

In fabrication, we have proposed a mesa structure for electrically-driven photonic crystal microcavity laser. According to this structure, we develop a series fabrication processes and all initial problems for mesa fabrication are solved, including defining the patterns of mesa, filling the isolation region with PR, and cleaning PR and SiNx by etching processes. We also setup a NIR micro-EL system for electrical driving, which can be used in examine the MQWs degradation during the mesa fabrication and electrically-driven laser emission. In the future, we will define 12-fold QPC D_2 microcavity on the mesa for electrical driving and electrically-driven photonic crystal microcavity laser with low threshold and high *Q* factor could be achieved by this structure.

4.2 Future Work

In the future, we will employ the mesa to fabricate the photonic crystal microcavity laser for electrically driven with central post. According to our simulation results, we investigate extra heat sink effect provided by the post by using FEM simulation without affecting $WG_{6,1}$ mode. We will fabricate the QPC D_2 microcavity with post size of 880μm for optical pumping.

And then we hope that the structure will achieve CW lasing.

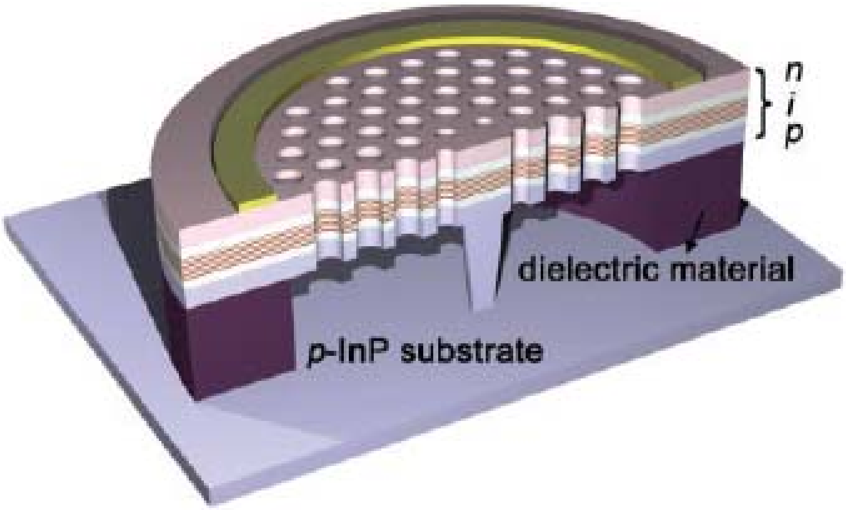

Fig. 4. 1: Diagram of electrically driven structure with central post by Hong-Gyu Park *et al* [12].

References

[1] E. Yablonovitch, *Phys. Rev. Lett.*, **vol. 58**, pp. 2059-2062, 1987.

[2] J. Limpert, T. Schreiber, A. Liem, S. Nolte, H. Zellmer, T. Peschel, V. Guyenot, and A. Tünnermann, “Thermo-optical properties of air-clad photonic crystal fiber lasers in high power operation,” Opt. Express **11**, pp. 2982-2990 (2003).

[3] T. D. Happ, A. Markard, M. kamp, A. Forchel, S. Anand, J.-L. Gentner, and N. Bouadma, *J. Vac. Sci Technol. B*, **vol. 19**, pp. 2775-2778, 2001

[4] M. Boroditsky, T. F. Karuss, R. Coccioli, R. Vrijen, R. Bhat, and E. Yablonovitch, *Appl.Phys. Lett.*, **vol. 75**, pp.1036-1038, 1999.

[5] S. Olivier, C. J. M. Smith, H. Benisty, C. Weisbuch, T. F. Krauss, R. Houdre, and U. Oesterle, *IEEE J. Quantum Electron*, **vol. 38(7)**, pp. 814-816, 2002.

[6] O. Painter, J. Vuckovic, and A. Scherer, *J. Opt. Soc. Amer. B*, **vol. 16**, pp. 275-285, 1999.

[7] H.-Y. Ryu, H.-G. Park, and Y.-H. Lee, *IEEE J. Select. Topics Quantum Electron.*, **vol. 4**, pp. 891-908, 2002.

[8] J. D. Joannopoulous, R. D. Meade, and J. N. Winn, *Princeton University Press*, 1995.

[9] Kengo Nozaki and Toshihiko Baba, “Laser characteristics with ultimate-small modal volume in photonic crystal slab point-shift nanolasers”, *Appl. Phys. Lett.* **88**, 211101 (2006)

[10] Eiichi Kuramochi,a_ Masaya Notomi, Satoshi Mitsugi, Akihiko Shinya, and Takasumi Tanabe, “Ultrahigh-*Q* photonic crystal nanocavities realized by the local width modulation of a line defect”, *Appl. Phys. Lett.* **88** 041112 (2006)

[11] S. L. McCall, A. F. J. Levi, R. E. Slusher, S. L. Pearton, and R. A. Logan, “Whispering

gallery mode microdisk lasers," Appl. Phys. Lett. **60**, 289-291 (1992).

[12] Hong-Gyu Park, Se-Heon Kim, Soon-Hong Kwon, Young-Gu Ju, Jin-Kyu Yang, Jong-Hwa Baek, Sung-Bock Kim, Yong-Hee Lee, " Electrically Driven Single-Cell Photonic Crystal Laser", *SCIENCE*, **305**, 1444-1447 (2004)

[13] Min-Kyo Seo, Kwang-Yong Jeong, Jin-Kyu Yang, and Yong-Hee Lee," Low threshold current single-cell hexapole mode photonic crystal laser", *Appl. Phys. Lett.* **90**, 171122 (2007)

[14] Hong-Gyu Park, Se-Heon Kim, Min-Kyo Seo, Young-Gu Ju, Sung-Bock Kim, and Yong-Hee Lee, "Characteristics of Electrically Driven Two-Dimensional Photonic Crystal Lasers", *IEEE J. Quantum Electron.* **41**, 1131-1141 (2005)

[15] Po-Tsung Lee, J. R. Cao, Sang-Jun Choi, Zhi-Jian Wei, John D. O'Brien, and P. Daniel Dapkus, "Operation of photonic crystal membrane lasers above room temperature", *Appl. Phys. Lett.* **81**, 3311-3313 (2002)

[16] Takashi Asano, Bong-Shik Song, Yoshihiro Akahane, and Susumu Noda," Ultrahigh-Q Nanocavities in Two-Dimensional Photonic Crystal Slabs", IEEE *J. Sel. Topics. Quantum Eelctron.* **12**, 1123-1134 (2006)

[17] Kengo Nozaki and Toshihiko Baba, "Laser characteristics with ultimate-small modal volume in photonic crystal slab point-shift nanolasers", *Appl. Phys. Lett.* **88**, 211101 (2006)

[18] M. H. Shih, Wan Kuang, Tian Yang, Mahmood Bagheri, Zhi-Jian Wei, Sang-Jun Choi, Ling Lu, John D. O'Brien,P. Daniel Dapkus, "Experimental Characterization of the Optical Loss of Sapphire-Bonded Photonic Crystal Laser Cavities", *IEEE Photon. Technol. Lett.* **18**, 535 (2006)

[19] Se-Heon Kim, Jae-Hoon Choi, Seung-Kon Lee, Shin-Hyun Kim,Seung-Man Yang, Yong-Hee Lee, Christian Seassal, PhilippeRegrency, Pierre Viktorovitch, "Optofluidic integration of a photonic crystal nanolaser", *Opt. Express* **16**, 6515 (2008)

[20] O. Painter, R. K. Lee, A. Scherer, A. Yariv, J. D. O'Brien, P. D. Dapkus, I. Kim, "Two-Dimensional Photonic Band-Gap Defect Mode Laser", *SCIENCE*, 284-286 (1999)

[21] Jeong-Ki Hwang, Han-Youl Ryu, Dae-Sung Song, Il-Young Han, Hyun-Woo Song, Hong-Kyu Park, and Yong-Hee Lee, "Room-temperature triangular-lattice two-dimensional photonic band gap lasers operating at 1.54 mm", *Appl. Phys. Lett.* **76**, 2982-2984 (2000).

[22] Po-Tsung Lee, J. R. Cao, Sang-Jun Choi, Zhi-Jian Wei, John D. O'Brien,and P. Daniel Dapkus," Room-Temperature Operation of VCSEL-Pumped Photonic Crystal Lasers", *Photon. Technol. Lett.* **14**, 435-437 (2002)

[23] Hong-Gyu Park, Jeong-Ki Hwang, Joon Huh, Han-Youl Ryu, Se-Heon Kim, Jeong-Soo Kim, and Yong-Hee Lee, "Characteristics of Modified Single-Defect Two-Dimensional Photonic Crystal Lasers", *IEEE J. Quantum Electron.* **38**, 1353-1365 (2002)

[24] Min-Kyo Seo, Kwang-Yong Jeong, Jin-Kyu Yang, and Yong-Hee Lee," Low threshold current single-cell hexapole mode photonic crystal laser", *Appl. Phys. Lett.* **90**, 171122 (2007)

[25] Hong-Gyu Park, Sun-Kyung Kim, Soon-Hong Kwon, Guk-Hyun Kim, Se-Heon Kim, Han-Youl Ryu, Sung-Bock Kim, and Yong-Hee Lee, "Single-Mode Operation of Two-Dimensional Photonic Crystal Laser With Central Post", *IEEE Photon. Technol. Lett.* **15**,1327-1329 (2003)

[26] Kengo Nozaki and Toshihiko Baba, "Quasiperiodic photonic crystal microcavity

lasers", *Appl. Phys. Lett.* **84**, 4875-4877 (2004)

[27] P. Strasser,a_ R. Wüest, and F. Robin, D. Erni, H. Jäckel, "Detailed analysis of the influence of an inductively coupled plasma reactive-ion etching process on the hole depth and shape of photonic crystals in InP/InGaAsP", *J. Vac. Sci. Technol. B*, **25**, 387-393 (2007)

[28] Han-Youl Ryu and Masaya Notomi, "High-quality-factor and small-mode-volume hexapole modes in photonic-crystal-slab nanocavities", *Appl. Phys. Lett.* **83**, 4294-4296 (2003)

[29] Takashi Asano, Bong-Shik Song, Yoshihiro Akahane, and Susumu Noda," Ultrahigh-Q Nanocavities in Two-Dimensional Photonic Crystal Slabs", IEEE *J. Sel. Topics. Quantum Eelctron.* **12**, 1123-1134 (2006)

[30] Sun-Kyung Kim, Jee-Hye Lee, Se-Heon Kim, In-Kag Hwang, and Yong-Hee Lee, "Photonic quasicrystal single-cell cavity mode" *Appl. Phys. Lett.* **86**, 031101 (2005)

Vita

Yi-Yu Tsai was born on 04 April, 1984 in I-Lan City, Taiwan. He received the B.S. degree from Department of Physics, National Central University, Chung Li, Taiwan in 2006. The M.S. degree will be received from Department of Photonics and Display Institute, National Chiao Tung University, Hsinchu, Taiwan in 2008. His researches focus on photonic crystal microcavity lasers.

Publication:

[01] Tsan-Wen Lu, Po-Tsung Lee, Chung-Chuan Tseng, and Yi-Yu Tsai, "Investigation of modal property and thermal behavior of high quality factor 12-fold quasi-photonic crystal microcavity with different central post sizes," Opt. Express 16, pp.12591-12598 (2008)